Available online at www.sciencedirect.com

Cement and Concrete Research 36 (2006) 1098 – 1107

3D surface image analysis for fracture modeling of cement-based materials

Anne B. Nichols [a,*], David A. Lange [b]

[a] Texas A&M University, Department of Architecture, College Station, TX 77843, USA
[b] University of Illinois, Department of Civil Engineering, Urbana, IL 61801, USA

Received 8 April 2005; accepted 10 January 2006

Abstract

The texture and exposed phases of a fracture surface are direct evidence of the mechanical behavior of a cement-based material. Deflection, microcracking and bridging are toughening mechanisms involved in fracture of brittle matrices that affect surface roughness. This study measures crack deflection and branching using 3D surface measurement techniques with confocal laser microscopy of mechanically fractured mortar prisms and 3D stereo pair microscopy of mechanically fractured plain concrete prisms. Image analysis techniques were used to identify phase composition and out-of-surface crack branching from profiles of cracks intruded with a low melting-point alloy. The resulting data was the basis for a micromechanical model to relate surface and phase data and the measured fracture energy to the increase in energy with respect to fracture of the matrix independent from the composite behavior.

Keywords: Image analysis; Microstructure; SEM; Fracture toughness; Micromechanics

1. Introduction

In order to understand the fracture behavior of complex cement-based composites, researchers have been drawn to a wide array of testing, imaging and modeling techniques [1]. One key interest is the energy consumed by fracture process and the role of toughening mechanisms [2]. Without access to direct observation of the toughening mechanics during fracture, the surface and near-surface evidence has been relied upon to study the microstructural response to strain [3]. Fracture models of crack opening behavior that rely on linear elastic fracture mechanics theories have been applied to provide some insight to the behavior of these non-linear elastic, quasi-brittle materials [2,4]. Imaging techniques such as laser-scanning confocal microscopy [5], 3D tomography [6], stereo microscopy and stereophotogramy [7] have been used to characterize a surface or volume from representative surface or section images of cement-based materials. Imaging of sections filled with various penetrants, including dyes and low-temperature molten metals, by optical or electrical microscopy such as scanning electron microscopy (SEM) or digital imaging, is useful for capturing “slices” of crack behavior [7–10]. Section images have been used extensively to characterize the phases and morphology of the microstructure [11,12].

The information collected by characterizing the surface geometry, phases and crack profiles has often been the basis for computational models. The surface tortuosity data alone has been used to correlate the roughness to mechanical properties [13,14], as well as to examine the relationship of scaling or fractal nature of the surface with the toughness [15]. Additional

Table 1
Mortar mix specifications

Set	No. of specimens	W/C	Cement/sand ratio by weight	Fluorescent dye (by weight water) (%)	Air entrainment (by weight cement) (%)	Fresh mortar air content (%)
A	6	0.5	1:1	5		0.82
B	6	0.5	1:1	5	0.3	3.57
C	6	0.5	1:2	5		1.85
D	6	0.5	1:2	5	0.3	7.70
E	6	0.5	1:1[a]	5		0.82

[a] Based on equivalent volume of ceramic balls.

---

* Corresponding author. Tel.: +1 979 845 6540; fax: +1 979 845 6540.
E-mail address: anichols@tamu.edu (A.B. Nichols).

0008-8846/$ - see front matter
doi:10.1016/j.cemconres.2006.01.002

Table 2
Concrete mix specifications

Set	No. of specimens	W/C	Water (kg/m^3)	Cement (kg/m^3)	Coarse aggregate^a (kg/m^3)	Fine aggregate a (kg/m^3)
Concrete	4	0.5	178 (300 lb/yd^3)	356 (600 lb/yd^3)	1197 (2018 lb/yd^3)	681 (1148 lb/yd^3)

[a] Surface saturated dry.

Table 3
Concrete aggregate properties

Coarse aggregate	Fine aggregate
TM=0.8%	TM=2.08%
AD=1.4%	AD=1.8%
$\gamma_{\mathrm{SSD}}=2.68$	$\gamma_{\mathrm{SSD}}=2.6$
Unit wt.$_{\mathrm{SSD}}$=101.40 lb/ft^3	FM=2.63

investigations have compared the interface transition zone roughness to fracture toughness in concrete [16]. Measurements of the orientation and volume fraction of aggregate have also been used to study effects of bridging at the crack face with respect to matrix–aggregate bond [17]. Models for the behavior of semi-brittle materials, such as ceramics with inclusions, have also been utilized to predict the strain energy release rate based on the influence of the deflection angle of the crack path [18]. Many models are limited to planar explorations of toughness although subsurface or 3D mechanisms such as branching are considered to contribute to the fracture energy.

This paper describes the fracture surface and profile characterization and image analysis methodology for obtaining data in the form of surface topology, crack branching measure and phase classification of the surface elements. This data is intended for use in micromechanical modeling that considers the effect of surface tortuosity and material phase properties on the strain energy release rate of mortar and concrete materials.

2. Experimental technique

To examine the relationship of microstructural geometry to fracture the test materials were designed with aggregate size, aggregate volume and entrained air as the variable parameters in order to examine the degree of porosity, induced cracks, crack deflection and crack plane. The test specimens where mechanically tested and the fracture evidence was prepared for examination of crack profiles and surfaces.

2.1. Materials

Five mixes were cast for the mortar specimens and one mix was cast for the concrete specimens. All mixes used Type I Portland Cement at a w/c ratio of 0.5. Florescent dye (propylene glycol monomethyl ether) was added at 5% by weight of water. The sand for the mortars was 20/30 ASTM C 778 silica sand. An air entraining agent was added at 0.3% by weight of cement. The aggregate for one set (E) was 0.79–1.18 mm alumina ceramic balls. The content of alumina balls in the mortar was based on the equivalent volume of silica sand for a 1:1 ratio of cement to sand by weight. The bulk densities of the silica sand and ceramic balls were measured as 1.755 g/cm^3 and 2.104 g/cm^3, respectively. The aggregate for the concrete was crushed limestone with maximum size of 3/4 in. and washed gravelly sand. The mortar mix specifications are presented in Table 1, and the concrete mix specification determined by the ACI 211.1 mix design method is presented in Table 2. The properties for the aggregates of the concrete are listed in Table 3. The fresh air content of the mortar was measured by ASTM C185 adjusted for silica sand content and is also presented in Table 1.

All mortar specimens were cast as 17.8 × 3.8 × 2.4 cm (7 × 1.5 × 1 in.) beams with a notch at midspan of 1.27 cm (Fig. 1). Set E was cast with mortar containing dye and alumina balls for the center 1.5 cm. The rest of the bar was cast with plain paste and no dye. All other mortar bars were cast and cured in the horizontal position.

The concrete specimens were cast as 71.1 × 15.2 × 10.2 cm (28 × 6 × 4 in.) beams with a notch at midspan of 5.1 cm (2 in.). The concrete beams were geometrically proportional to the mortar beams by a factor of 4.

All specimens were cured in laboratory conditions for 1 day and then moist cured for a total of 14 days prior to mechanical testing of the notched beams in three-point bending using the RILEM two-parameter fracture model method [19]. Four beams from each mortar and concrete set were loaded to separation after completion of mechanical testing. Two beam of each mortar set were loaded to 75% and 85% of peak load on the second loading cycle and a wedge was inserted into the cast notches to keep the cracks from closing.

2.2. Crack infiltration

To prepare the mortar beams with remaining crack ligaments for intrusion, sections were removed at midspan through the

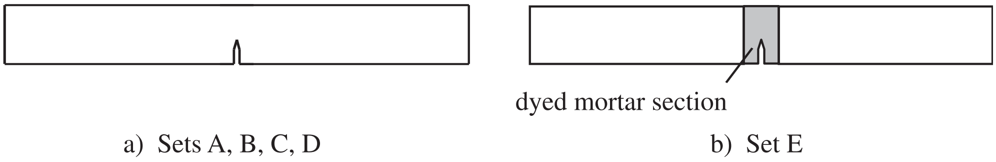

a) Sets A, B, C, D b) Set E

Fig. 1. Mortar bar geometry.

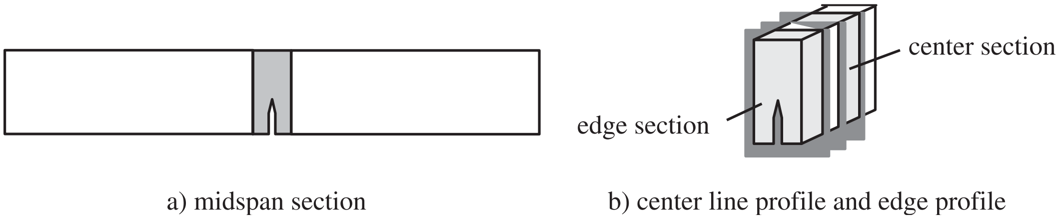

Fig. 2. Crack section geometry.

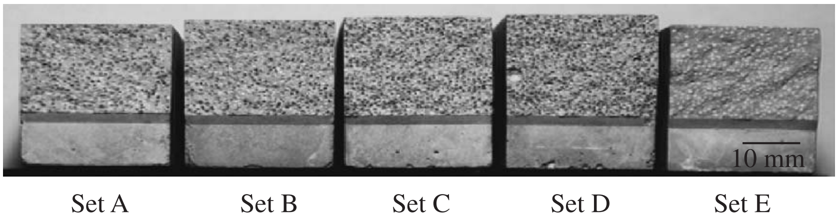

Fig. 3. Typical fracture surfaces of mortar beams.

cross section (Fig. 2a). These pieces were then sectioned into a center profile and an edge profile (Fig. 2b), which were generally 1 cm wide. The specimen samples were oven dried (105 °C) prior to intrusion.

The intrusion procedure was derived from the intrusion porosimetry technique involving Wood's metal, an alloy with a low melting point, used by Willis et al. [20] Wood's metal is comprised of bismuth, lead, tin and cadmium, and has a freezing point near 66 °C with no appreciable volume change. The mortar specimens and Wood's metal were loaded into an autoclave, which was evacuated, heated above 90 °C, pressurized to 10.3 MPa (1500 psi) and allowed to cool to room temperature.

2.3. Confocal microscopy

A laser-scanning confocal microscope was used to optically obtain surface elevation data and images containing phase information using reflective laser light under non-fluorescing and fluorescing conditions for the fracture surfaces of the mortar specimens (Fig. 3). The confocal microscope records a series of optical sections at different focal planes and constructs a digital image in which each pixel is assigned a value that represents the z level of the in-focus plane. The elevation data contained in the images can be used to recreate the surface or profiles visually or numerically. The 256 × 512 pixel digital images contain the topographic map in the top half and the confocal image, which appears as a focused image of the surface, in the bottom half (Fig. 4).

The images were acquired with an argon laser source and red-detecting photomultiplier using square pixels, a 2.5× lens at 20 times for a 50× magnification, and a fluorescent filter for the fluorescent imaging. A square matrix of 16 images on each surface were required to provide a 95% degree of confidence and confidence interval of 8% based on the standard deviation of the roughness number (a measure of surface roughness) from previous measurements on a mortar with the same aggregate size and distribution [21]. The field size for the images was approximately 3.5 mm × 3.5 mm (0.0138 mm/pixel). The z slice thickness was 13.5 µm. The confocal microscope scanned the surface once per z elevation. Contrast and brightness was controlled to avoid saturation of dark or bright areas (low and high) resulting in artificially flat topography. Saturation did occur on or around the aggregate due to the faceted features of the silica grains in 15% of the image pixels. This reflection of the laser light could not be directed or identified as noise and image filtering was necessary to interpolate the missing data [22].

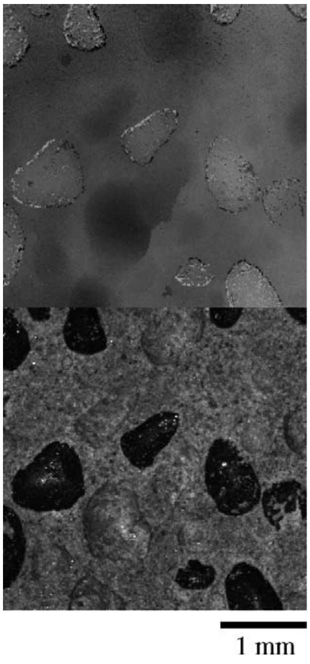

Fig. 4. Data file of range image (top) and confocal image (bottom).

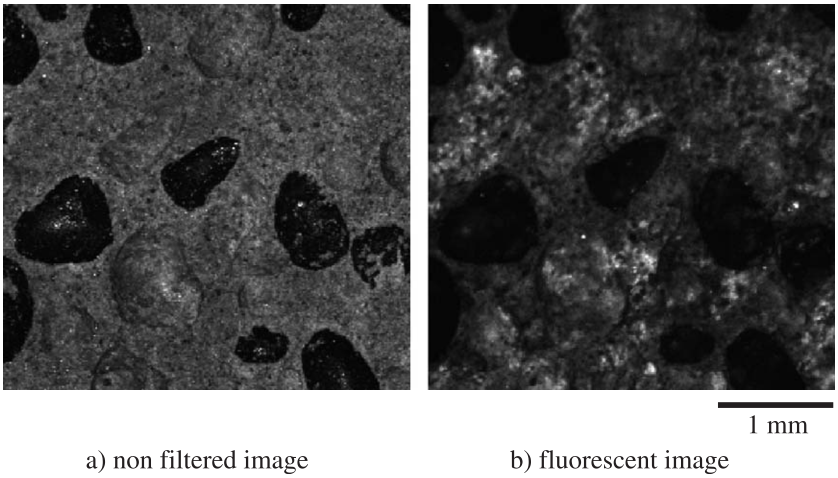

a) non filtered image b) fluorescent image

Fig. 5. Confocal images.

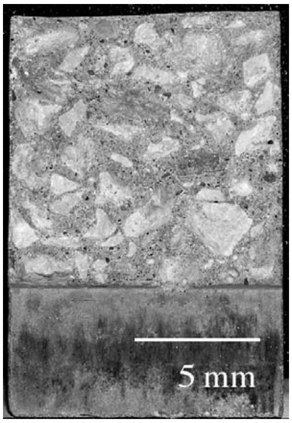

Fig. 6. Typical fracture surface of concrete beams.

Images were also taken with the fluorescent filter of the identical area as the elevation image. The contrast and brightness for the fluorescent images were controlled to saturate the dark values recorded for the non-reflecting aggregates. Fig. 5 shows a pair of confocal images without the filter and with the fluorescent filter.

The confocal images and corresponding fluorescent images were analyzed to identify aggregates, broken aggregates, impressions of where aggregates had been, as well as to identify visible voids and pore spaces.

2.4. 3D stereo pair microscopy

A 3D stereo pair microscopy evaluation was performed on the mortars and concrete fracture surfaces to measure elevations based on a shift of the optical focal point as a point of comparison and because of the range limitation of the laser-scanning confocal technique. The fracture surfaces of the mortar specimens and concrete specimens (Fig. 6) were imaged as stereo pairs with a scanning electron microscope, and a CCD video camera and software, respectively. Example pairs are shown in Fig. 7. The pairs simulate how we perceive depth with our eyes. The right side images are the result of tilting the stage of the microscope or camera. The difference in depth from a reference plane can be determined based on the shift between

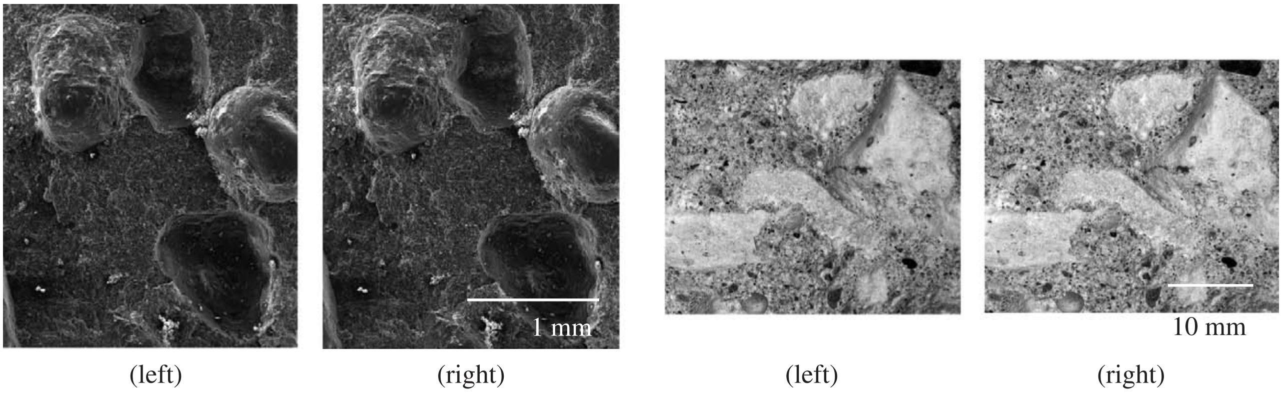

a) mortar stereo pair (50X) b) concrete stereo pair (4X)

Fig. 7. Surface stereo pairs.

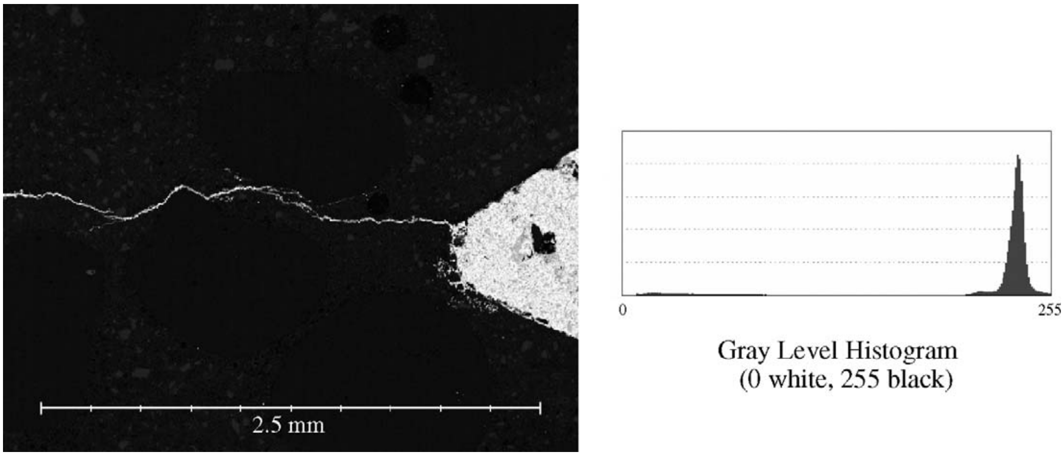

Fig. 8. Sample BSE micrograph of crack profile (50×) and histogram of gray values.

Fig. 9. Complete edge crack profile for mortar sample A6 (50×).

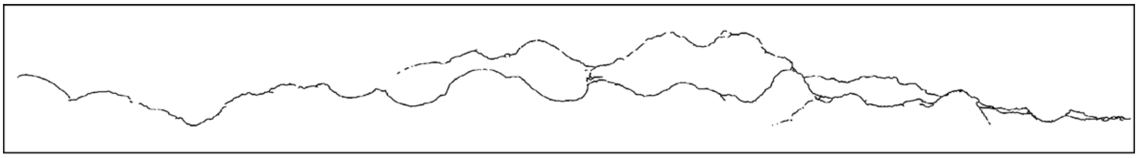

(a) full crack profile

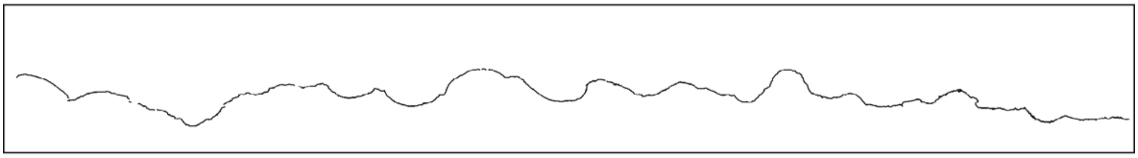

(b) crack profile without branching

Fig. 10. Full crack profile and profile with branches removed (field width 15.86 mm).

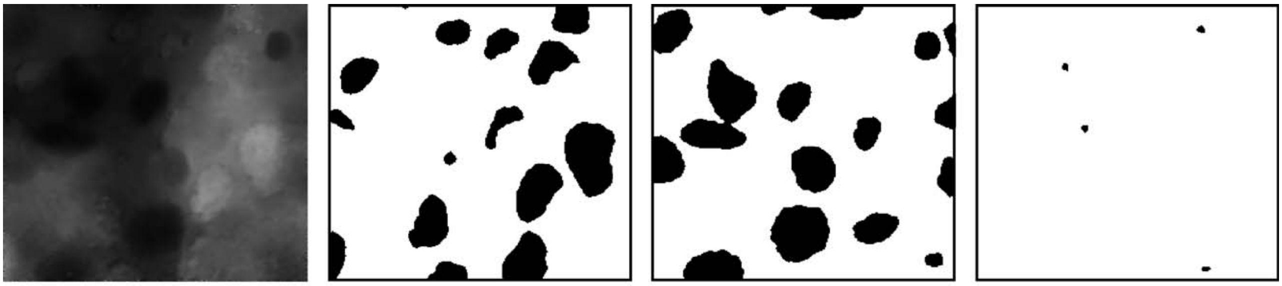

a) range image b) aggregates c) aggregate impressions d) voids

Fig. 11. Example stack images for a mortar confocal image.

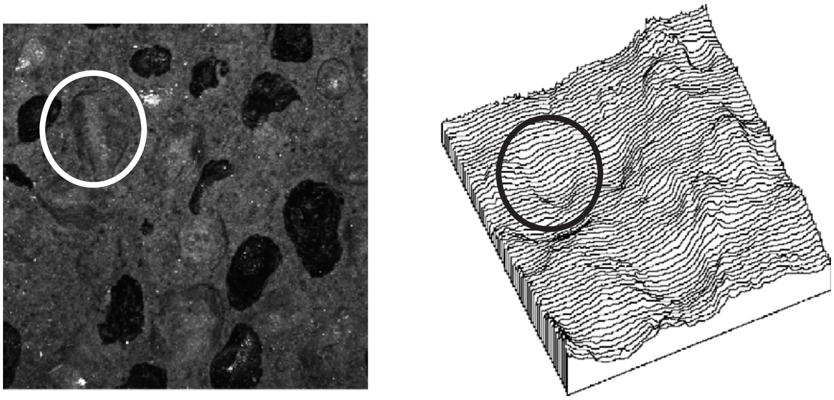
a) aggregate impression feature in confocal image

b) aggregate impression in range plot

Fig. 12. Aggregate impression characterization.

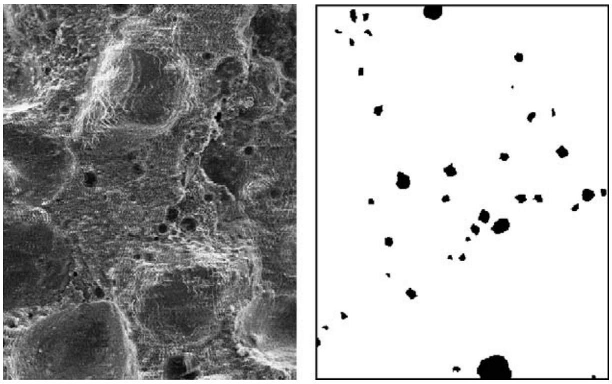
a) stereo composite image in grayscale

b) void binary image

Fig. 13. Void identification for a mortar 3D stereo image.

left and right stereo images and the stage tilt angle at a constant focal length.

Five images were taken for each fracture surface. The location for the images taken on each sample was at each corner and the center of the surface.

The 3D stereo pair images were processed using software programs included with the IMIX imaging system[1]. The text files of x,y,z grid point values were assembled and converted to binary range files. The left stereo image taken at 0° tilt was used for image analysis to identify aggregates, aggregate impressions, broken aggregates, and visible voids and pore spaces.

3. Image analysis

3.1. Crack profile

To extract information about the crack geometry, the intruded crack specimens were imaged and processed with a series of image analysis steps to obtain a discrete crack centerline. The two intruded crack sections from each unfractured mortar beam were imaged using BSE microscopy. The high atomic weight of the Wood's metal alloy, compared to the cement phases and silica sand, provided sharp contrast in backscatter mode. A typical crack segment image and corresponding histogram are presented in Fig. 8. The silica sand grains appear the darkest, the cement paste matrix is a lighter gray, and the Wood's metal is bright. The backscatter

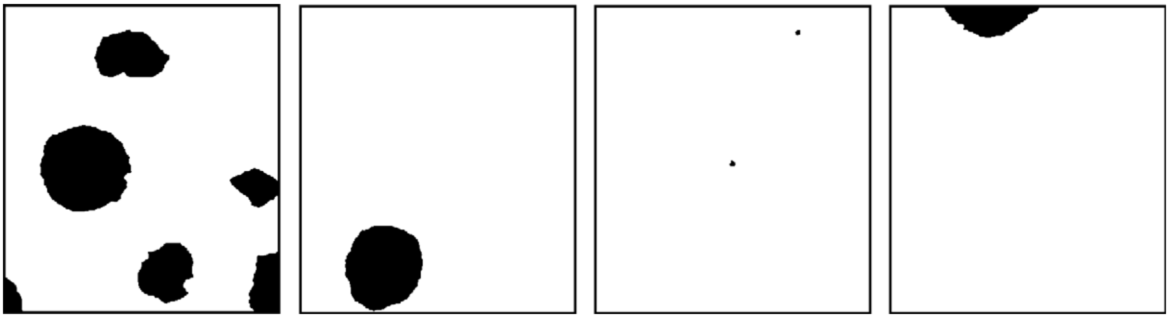
a) aggregates

b) aggregate holes

c) voids

d) broken aggregates

Fig. 14. Example stack binary images for a 3D stereo mortar image.

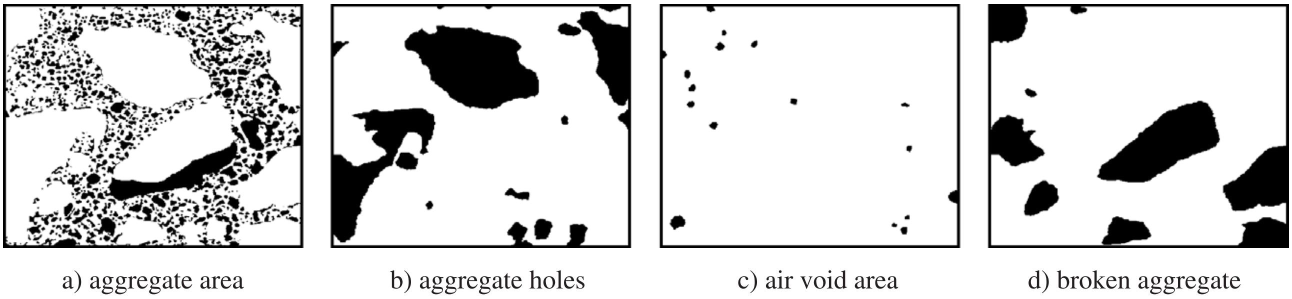

Fig. 15. Example stack binary images for a 3D stereo concrete image.

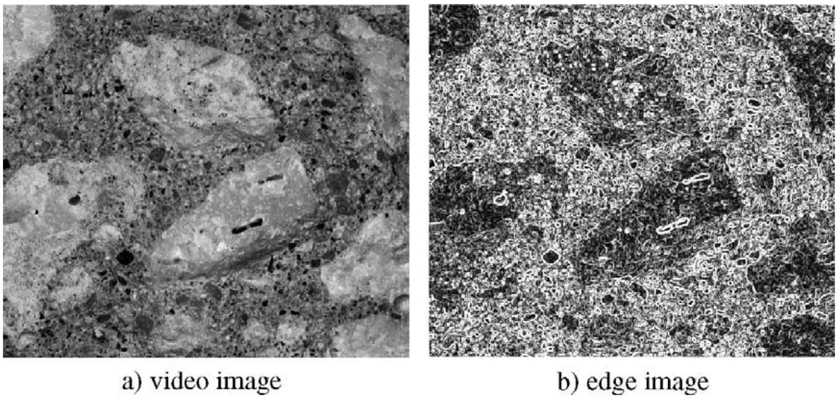

Fig. 16. Concrete video image and edge image.

images along the crack of each sample were captured digitally at 50× and were stitched to create a complete crack image. An example is shown in Fig. 9.

The micrographs revealed imperfect filling of cracks, possibly due to residual water vapor pressure present during molten metal intrusion. To obtain the complete crack profile, an additional image process was used. The unfilled crack segments (very dark areas) were added to the filled crack segments (very bright areas) to create the full crack profile. The crack thickness was reduced to a single pixel-wide line with a skeletonizing function for the completed line profile. The branching cracks were removed and the line profile without branching was recorded. Example profiles of complete crack and crack without branching are shown in Fig. 10.

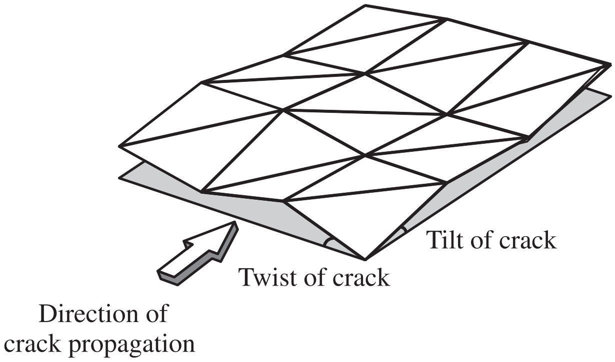

Fig. 17. Surface schematic for micromechanical model.

3.2. Mortar phase separation

For both the confocal images and the SEM micrographs of the mortar specimens, a series of image analysis steps were performed to identify areas of paste, aggregate, aggregate impressions and voids as shown in Fig. 11. The fluorescent confocal image from the bottom half of the 512×256 pixel digital image was used to identify the aggregate area on the surface. The contrast and brightness of the image was enhanced to distinguish the aggregate and a threshold was applied to identify the aggregates as black to construct a binary image (Fig. 11b).

The binary representation of the areas of aggregate impressions was determined by using a gray density slice function and binary conversion of the resulting image to isolate the edge outline. Fig. 12 illustrates the aggregate impression feature and the profile in the range image. The binary

Table 4
Average crack measurements and branching ratio for mortar specimens

Sample set	Length of main crack (pixels)	Length of branches (pixels)	Total length (pixels)	Branching ratio (total/main crack)
A	2261	470	2731	1.21
B	2632	681	3313	1.27
C	4277	2659	6939	1.66
D	2914	1092	4006	1.36
E	2626	449	3075	1.17

Table 5
Mortar confocal and 3D image analysis area measurements

	Cement paste area (%)		Sand area (%)		Air area (%)	
	Confocal	3D	Confocal	3D	Confocal	3D
Set A	68.26	65.09	31.14	33.02	0.60	1.89
Set B	70.42	63.35	27.56	33.75	2.02	2.89
Set C	56.26	52.23	41.90	46.85	1.84	0.92
Set D	52.76	51.51	41.06	40.82	6.18	7.67
Set E	75.28	72.70	23.85	26.50	0.87	0.80

representation of voids and pores was constructed in the same manner.

The filtered range image, aggregate binary, hole binary and void binary images were combined into an image stack file. Fig. 12 shows an example of binary files corresponding to a confocal range image.

The composite image of each left, right 3D stereo pair (Fig. 13a) was used to identify the areas of intact aggregate, broken aggregate, aggregate impressions and visible voids on the surface. Image analysis using a range of thresholding values was performed to identify edge boundaries. Aggregate areas were identified first with respect to the composite image and stored in a binary file. When areas of broken aggregate were identified, the area was removed from the aggregate binary and added to the broken aggregate binary for the sample. For determining the void area, the pixel space not containing aggregates or aggregate impressions was used to identify edge boundaries as described. Fig. 13 illustrates the composite image and the resulting void binary image.

The aggregate binary, broken aggregate binary, hole binary and void binary were combined into an image stack file. Fig. 14 shows an example of binary files corresponding to the range data for a mortar 3D stereo pair. The confocal image stack file for the mortar data did not include a broken aggregate binary image.

3.3. Concrete phase separation

For the video images of the concrete, a series of image analysis steps were performed to identify areas of paste, aggregate, aggregate impressions and voids (Fig. 15). Image analysis was used to identify the aggregate areas using the maximum value found by an edge detector kernel for each of eight directions around a pixel. Fig. 16 illustrates the video image and resulting edge image.

Table 6
Mortar 3D image analysis area measurements and mix design volumes

	Cement paste volume (%)		Sand volume (%)		Air volume (%)	
	Mix	Images	Mix	Images	Mix	Images
Set A	49.79	65.09	49.39	33.02	0.82	1.89
Set B	51.39	63.35	47.71	33.75	3.57	2.89
Set C	24.28	52.23	73.87	46.85	1.85	0.92
Set D	22.47	51.51	69.83	40.82	7.70	7.67
Set E	58.27	72.70	40.91	26.50	0.82	0.80

The edge detection did not discriminate between variations of composition within a large aggregate. One or two opening operations were performed on the edge image such that the very small outlines were removed from within the large aggregate shapes. The fine aggregate particles were identified from the edge image area excluding large aggregate areas using a series of thresholding operations and additions. Fig. 16a shows the thresholded edge image. A series of erosions with different neighboring pixel counts were applied to clean the image of single pixels not identified with any aggregate.

The binary images of broken aggregates, aggregate holes and visible voids were determined in the same manor as presented for the mortar specimen images. These images were combined into an image stack file. Fig. 15 shows an example of binary files corresponding to the range data for a concrete 3D stereo pair.

4. Results

4.1. Crack branching measurement

The linearized crack profiles were measured using the relationship:

$$\text{Length} = 0.948 \times (\text{num. of orthogonal neighbors}) + 1.340 \times (\text{num. of diagonal neighbors}) \qquad (1)$$

where the number of orthogonal and diagonal neighbors were measured by scanning rows of the profile image. The results for the mortar specimens are presented in Table 4. The calculated branching ratios did not show a relationship between the amount of branching and the location through the cross section or to the load value at unloading. The ratios tended to be higher for the center section than for the edge section but still indicate that the assumed condition of plain strain was valid.

4.2. Phase area fractions

The area fractions calculated for the confocal images of mortar are presented with those calculated for the SEM images in Table 5. The image analysis shows good agreement between microscopy method and image analysis techniques for phase identification.

Area fraction calculations were performed on the phase binaries for the mortar 3D stereo pairs. The area fractions correlate with volume fractions. The results for the mortar sample sets are reported in Table 6 along with the volume

Table 7
Concrete 3D mix design volumes and image analysis volume measurements

Cement paste volume (%)		Aggregate volume (%)		Sand volume (%)		Air volume (%)	
Mix	Images	Mix	Images	Mix	Images	Mix	Images
27.73	41.49	44.78	35.98	26.49	21.31	1.00	1.22

fractions determined from mix weight fractions and measurement. The measured aggregate volume fractions are consistently lower than those from mix weight fractions, as was seen with the confocal images, because of the bias toward the paste.

Area fraction calculations were performed on the phase binaries for the 3D stereo pair images of concrete. The results are reported in Table 7 along with the volume fractions determined from mix weight fractions and measurement. The measured aggregate volume fractions are consistently lower than those from mix weight fractions, as was seen with the mortar images, because of the bias toward the paste.

4.3. Application in micromechanical modeling

The result of the characterization and image analysis of crack branching ratio plot fit, range elevations and binary image stacks are essential geometric and morphological information required in a micromechanical model of fracture. The model determines an average strain energy release rate based on the tilt and twist angles of the crack path and the Young's modulus of the phases on the crack segment (matrix, aggregate, interface or void). The local angle of tilt along the crack progression is determined from the change in elevation between progressive pixels in the binary range image representing surface geometry, while the local angle of twist is determined from the change in elevation between orthogonal pixels (illustrated in Fig. 17). The local strain energy release rate can be determined from the local stress intensity factors that are a function of Poisson's ratio, the unknown flat crack stress intensity factor, trigonometry of the angles and the Young's modulus of the crack segment whose phase is determined from the corresponding binary phase images within the stack. When a crack segment spans two phases, the segment is considered to be interfacial paste. The average strain energy release rate for the surface with respect to that of a flat crack can be determined and subsequently magnified with the branching ratio (taking into account the subsurface cracking) in order to identify the critical stress intensity factor for a theoretical flat crack in the matrix, in essence, extracting the contribution of tortuosity and inclusions from the composite strain energy release rate [22].

5. Summary

The research describes the image acquisition of mortar and concrete fracture surfaces using confocal laser microscopy, fluorescence, video and scanning electron microscopy to obtain fracture surface morphology and geometry. An intrusion technique using Wood's metal allowed crack profiles perpendicular to the fracture surface to be captured with backscatter electron microscopy. Image analysis was performed on the crack micrographs to identify a measure of crack branching, while confocal images and the 3D stereo pairs from video and electron microscopy were used to identify areas of aggregate, paste, voids, broken aggregates and aggregate impressions. The resulting binary and range maps were data required for a micromechanical model, which can calculate an average strain release rate based on the angle and phase of crack segment in addition to the increase in toughness with respect to subsurface crack branching.

The image analysis solution presents a quantifiable method of obtaining surface morphology and subsurface cracking that can be related directly to the mechanisms of crack branching and deflection in cement-based materials.

Acknowledgements

This research was supported by the NSF Center for Advanced Cement-Based Materials (NSF Grant No. DMR 88808432-01).

References

[1] S. Mindess, The cracking and fracture of concrete: an annotated bibliography, in: F.H. Wittmann (Ed.), Fracture Mechanics of Concrete, Elsevier, Amsterdam, 1983.

[2] A. Hillerborg, The theoretical basis of a method to determine the fracture energy GF of concrete, Mater. Struct. 18 (106) (1985) 291–296.

[3] S.P. Shah, C. Ouyang, Measurement and modeling of fracture processes in concrete, in: J. Skalny (Ed.), Materials Science of Concrete, vol. III, The American Ceramic Society, OH, 1992.

[4] Y. Jenq, S.P. Shah, A two parameter fracture model for concrete, J. Eng. Mech. 111 (10) (1985) 1227–1241.

[5] D.A. Lange, H.M. Jennings, S.P. Shah, Relationship between fracture surface roughness and fracture behavior of cement paste and mortar, J. Am. Ceram. Soc. 76 (3) (1993) 589–597.

[6] E.N. Landis, S.P. Shah, Influence of microcracking on the mechanical behavior of cement based materials, Adv. Cem. Base Mater. 2 (3) (1996) 105–118.

[7] S. Mindess, S. Diamond, SEM investigations of fracture surfaces using stereo pairs: II. Fracture surfaces of rock-cement paste composite specimens, Cem. Concr. Res. 22 (4) (1992) 678–688.

[8] S. Mindess, S. Diamond, The cracking and fracture of mortar, Mater. Struct. 15 (86) (1982) 107–113.

[9] A. Bascoul, A. Turatsinze, Microstructural characterization of mode I crack opening in mortar, Mater. Struct. 27 (166) (1994) 71–78.

[10] K.M. Nemati, P.J.M. Monteiro, A new method to observe three-dimensional fractures in concrete using liquid metal porosimetry technique, Cem. Concr. Res. 27 (9) (1997) 1333–1341.

[11] K.L. Scrivener, The use of backscattered electron microscopy and image analysis to study the porosity of cement paste, Mater. Res. Soc. Symp. Proc. 137 (1989) 129–140.

[12] K.L. Scrivener, H.H. Patel, P.L. Pratt, L.J. Parrott, Analysis of phases in cement paste using backscattered electron images, methanol adsorption and thermogravimetric analysis, Mater. Res. Soc. Symp. Proc. 85 (1987) 67–76.

[13] M.A. Issa, A.M. Hammad, A. Chudnovsky, Correlation between crack tortuosity and fracture toughness in cementitious material, Int. J. Fract. 60 (2) (1993) 97–105.

[14] D.A. Lange, H.M. Jennings, S.P. Shah, Relationship between fracture surface roughness and fracture behavior of cement paste and mortar, J. Am. Ceram. Soc. 3 (76) (1993) 589–597.

[15] M.A. Issa, A.M. Hammad, Fractal characterization of fracture surfaces in mortar, Cem. Concr. Res. 23 (1) (1993) 7–12.

[16] D. Zampini, H.M. Jennings, S.P. Shah, Characterization of the paste-aggregate interfacial transition zone surface roughness and its relationship to fracture toughness of concrete, J. Mater. Sci. 30 (12) (1995) 3149–3154.

[17] E. Schlangen, J.S.M. van Mier, Simple lattice model for numerical simulation of fracture of concrete materials and structures, Mater. Struct. 25 (152/153) (1992) 534–542.

[18] A.B. Abell, D.A. Lange, Fracture mechanics modeling using images of fracture surfaces, Int. J. Solids Struct. 35 (31–32) (1997) 4025–4034.

[19] RILEM Draft Recommendations, TC89-FMT fracture mechanics of concrete—test methods, determination of fracture parameters (K_{Ic}^{S} and $CTOD_c$) of plain concrete using three-point bend tests, Mater. Struct. 23 (1990) 457–460.

[20] K.L. Willis, A.B. Abell, D.A. Lange, Image based characterization of cement pore structure using wood’s metal intrusion, Cem. Concr. Res. 28 (12) (1998) 1695–1705.

[21] A.B. Abell, D.A. Lange, Image-based characterization of fracture surface roughness, Mater. Res. Soc. Symp. Proc. 370 (1994) 107–114.

[22] A.B. Abell, PhD dissertation, University of Illinois, Urbana-Champaign, IL, 2000.